



# Insight into the efficient oxidation of methyl-ethyl-ketone over hierarchically micro-mesostructured Pt/K-(Al)SiO<sub>2</sub> nanorod catalysts: Structure-activity relationships and mechanism

Zeyu Jiang<sup>a</sup>, Chi He<sup>a,b,\*</sup>, Nicholas F. Dummer<sup>b</sup>, Jianwen Shi<sup>c</sup>, Mingjiao Tian<sup>a</sup>, Chunyan Ma<sup>d</sup>, Zhengping Hao<sup>d</sup>, Stuart H. Taylor<sup>b</sup>, Mudi Ma<sup>a</sup>, Zhenxing Shen<sup>a</sup>

<sup>a</sup> Department of Environmental Science and Engineering, State Key Laboratory of Multiphase Flow in Power Engineering, School of Energy and Power Engineering, Xi'an Jiaotong University, Xi'an 710049, Shaanxi, PR China

<sup>b</sup> Cardiff Catalysis Institute, School of Chemistry, Cardiff University, Main Building, Park Place, Cardiff, CF10 3AT, UK

<sup>c</sup> Center of Nanomaterials for Renewable Energy, State Key Laboratory of Electrical Insulation and Power Equipment, School of Electrical Engineering, Xi'an Jiaotong University, Xi'an 710049, Shaanxi, China

<sup>d</sup> Department of Environmental Nano-materials, Research Center for Eco-Environmental Sciences, Chinese Academy of Sciences, Beijing 100085, PR China

## ARTICLE INFO

### Keywords:

Monodispersed Pt sites  
Al-K decorated silica  
Methyl-ethyl-ketone  
Catalytic oxidation  
Activation mechanism

## ABSTRACT

Hierarchically micro-mesostructured Pt/K-Al-SiO<sub>2</sub> catalysts with regular nanorod (Pt/K-A-NRS) and spherical nanoflower-like (Pt/K-A-SNFS) morphologies were prepared. The existence of Al atoms generates Brønsted acid sites and reduces silanol groups over the supports, promoting the dispersion of Pt nanoparticles and stability of catalysts. Potassium atoms balance the negative charge of supports and enhance O<sub>2</sub> mobility. The Pt/K-A-NRS catalysts exhibit unexceptionable low temperature activity, CO<sub>2</sub> selectivity, and stability for MEK oxidation. Amongst, 0.27 wt.% Pt/K-A-NRS completely converts MEK at just 170 °C (activation energy as low as 37.22 kJ·mol<sup>-1</sup>), more than 100 °C lower than other typical Pt/Pd supported catalysts reported in the literature. Diacetyl and 2,3-butandiol are the main intermediates during MEK activation, which convert into H<sub>2</sub>O and CO<sub>2</sub> through aldehydes and acids. The excellent catalytic activity of Pt/K-A-NRS is ascribed to their regular morphology, high Pt<sup>0</sup> content and dispersion, excellent MEK adsorption capacity and superior O<sub>2</sub>/CO<sub>2</sub> desorption capability under low temperature.

## 1. Introduction

Volatile organic compounds (VOCs) are one of the major contributors to air pollution, and harmful to human health and the environment due to the formation of photochemical smog, secondary aerosols and potential toxicity including carcinogenicity [1]. The most common VOCs are halogenated compounds, such as aldehydes, alcohols, ketones and aromatic compounds, which can be divided into outdoor sources and indoor sources [2,3]. Methyl-ethyl-ketone (MEK) is typical of oxygenated VOCs due to their widely use as a solvent in many large-scale processes such as printing and manufacturing [4]. Complete catalytic oxidation is a promising way to dispose VOCs, especially with low concentration (< 0.5 vol.%), into CO<sub>2</sub> and water [5]. However, this reaction should to proceed at low temperatures for the consideration of safety, energy saving, low cost and reduced environmental impact [6]. The development of highly efficient and promising catalysts for

abatement of VOCs at low temperatures continues to attract considerable attention. Generally, there are three major types of catalysts developed for VOC oxidation; supported noble metal catalysts, transition metal oxides, and a combination of these [7,8]. Among these examples, the noble metal based catalysts are preferred because of their high specific activity, resistance to deactivation and ability to be regenerated [9]. Among the supported noble metals, platinum, gold, palladium, and silver have been extensively studied for VOC oxidation.

The catalytic performance of supported noble metal catalysts strongly depends on the preparation method, type of precursor, metal morphology, particle size, and nature of the support, all of which impact the deposition and particle dispersion of active elements so as to impact the properties of catalysts. For example, the hierarchical nature of the porous network provides a larger surface area for better dispersion of the deposited active phase and offers the possibility to obtain a smaller active phase [10,11]. Therefore, lots of hierarchically

\* Corresponding author at: Department of Environmental Science and Engineering, State Key Laboratory of Multiphase Flow in Power Engineering, School of Energy and Power Engineering, Xi'an Jiaotong University, Xi'an 710049, Shaanxi, PR China.

E-mail address: [chi\\_he@xjtu.edu.cn](mailto:chi_he@xjtu.edu.cn) (C. He).

<https://doi.org/10.1016/j.apcatb.2017.12.007>

Received 25 August 2017; Received in revised form 30 November 2017; Accepted 4 December 2017

Available online 10 December 2017

0926-3373/© 2017 Elsevier B.V. All rights reserved.

structured pure silica materials have been widely used as supports for noble metal-based catalysts [10]. However, pure silica materials have an electrically neutral framework and consequently lack acid sites, which impede development as a support for highly effective catalysts. The acid sites of catalyst are relevant to metal dispersion and adsorption/desorption of reactants and CO<sub>2</sub> [12]. It is expected that the addition of aluminum yields so-called structural hydroxyls which can serve as Brønsted acid sites through tetrahedral coordination to four silicon atoms via oxygen bridges. Chen et al. increased the Al loading in a Beta zeolite framework which significantly improves the activity for the catalytic removal of toluene [13].

The morphology and crystal plane of the support also have significant effects on catalytic activity of supported noble metal catalysts. Huang et al. confirmed that the activity of Ru/CeO<sub>2</sub> catalysts for chlorobenzene oxidation is greatly affected by ceria morphology and crystal plane [14]. Additionally, the presence of potassium atoms in catalysts has a positive impact on their oxidation performance. Li et al. proposed that a well-dispersed Pd species was formed in the case of a Pd-K/TiO<sub>2</sub> catalyst due to a stabilizing effect by alkali metal cations, which facilitated the activation of chemisorbed oxygen [15]. The promotion effect of alkali-metal on the activity Pt/TiO<sub>2</sub> in formaldehyde deep oxidation was further proposed by Zhang and co-workers [16].

The potential application of Pt and Pd supported catalysts for oxidation of MEK has been hindered with high noble metal loading, inferior MEK activation capability, low CO<sub>2</sub> selectivity and production of hazardous by-products [17–19]. Arzamendi et al. revealed that the temperature for complete oxidation of MEK was as high as 370 °C over 1.0 wt.% Pd/Al<sub>2</sub>O<sub>3</sub> catalyst [17]. Gil et al. fabricated a 2.3 wt.% Pt/Al-pillared clay (BAsep) catalyst for catalytic combustion of MEK, while the high Pt content led to poorly dispersed metallic platinum, resulted in an inferior oxidation performance with 90% of MEK (600 ppm) converted at 265 °C [18]. Guillemot et al. stated that complete CO<sub>2</sub> selectivity for MEK incineration over a 1.0 wt.% Pt/NaX catalyst did not occur and reaction byproducts were probably formed [19]. In our previous work, we also revealed that a great number of unfavorable reaction by-products during MEK destruction were formed [20,21]. In addition, the irregular microstructure of these supports may have unanticipated impacts on the homogeneity of the active sites and the long-term stability of catalysts. Therefore, the development of novel supported noble metal catalysts with monodispersed noble metal active sites located on regular supports for efficient MEK destruction at low temperature is of great interest to researchers.

In this work, nanorod silica (NRS) supports with large specific surface area, enhanced micropore volume, and uniform pore structure were creatively synthesized by a hydrothermal and dual-surfactant strategy. The synthesized materials were then aluminated and doped with K to obtain K-(Al) nanorod silica (KA-NRS), over which monodispersed Pt nanoparticles with an average diameter of *ca.* 2.4 nm were deposited. We found that the Pt/KA-NRS catalysts possess outstanding MEK oxidation performance. Amongst, 0.27 wt.% Pt/KA-NRS can completely destruct 800 ppm of MEK at just 170 °C with a CO<sub>2</sub> selectivity higher than 90%, which is the best result regarding MEK catalytic oxidation to our knowledge. Furthermore, we investigated the MEK destruction routes and activation mechanism by *in situ* DRIFTS and DFT studies. We propose that the Pt/KA-NRS catalyst should be a promising candidate for VOC efficient catalytic elimination.

## 2. Experimental

### 2.1. Catalyst preparation

The spherical nanoflower-like silica (SNFS) and nanorod silica (NRS) were synthesized according to the previous work (Text S1, Supplementary Material), and the formation mechanisms of SNFS and NRS can be found in Fig. S1 and S2. The recovered silica materials were aluminated through the grafting method with anhydrous AlCl<sub>3</sub> and then

ion exchanged with an aqueous solution of 2 M KCl, which are referred to KA-SNFS and KA-NRS. Polyvinylpyrrolidone (PVP) capped Pt nanoparticles were synthesized and supported on KA-SNFS and KA-NRS by the ethylene glycol reduction method and colloid impregnation method (see Supplementary Material). The final catalysts were denoted as Xwt.% Pt/KA-NRS and Xwt.% Pt/KA-SNFS (X represents the actual content of Pt measured by ICP-OES). The Pt/MCM-41 and Pt/γ-Al<sub>2</sub>O<sub>3</sub> samples were further prepared by wetness impregnation (WI) method (see Supplementary Material).

### 2.2. Catalyst characterizations

The synthesized samples were systematically characterized by X-ray diffraction (XRD), low-temperature N<sub>2</sub> adsorption-desorption, inductively coupled plasma optical emission spectrometry (ICP-OES), hydrogen and oxygen titration (HOT), field emission scanning electron microscopy (FE-SEM), high resolution transmission electron microscopy (HR-TEM), high-angle annular dark-field imaging in the scanning transmission electron microscopy (HAADF-STEM), hydrogen temperature-programmed reduction (H<sub>2</sub>-TPR), oxygen temperature-programmed desorption (O<sub>2</sub>-TPD), MEK temperature-programmed desorption (MEK-TPD), CO<sub>2</sub> temperature-programmed desorption (CO<sub>2</sub>-TPD), FT-IR spectroscopy for NH<sub>3</sub> adsorption (NH<sub>3</sub>-IR), FT-IR spectroscopy for CO adsorption, Fourier transform infrared spectroscopy (FT-IR), X-ray photoelectron spectroscopy (XPS), ultraviolet-visible spectroscopy adsorption spectra (UV-vis), Raman spectra (Raman), electron spin resonance spectra (ESR), temperature programmed surface reaction (TPSR), *in situ* DRIFTS and DFT studies. The detailed methods for each technique are described in the Supplementary Material.

### 2.3. Catalytic activity

The catalytic performance for MEK oxidation was performed in a continuous-flow fixed-bed reactor, consisting of a steel tube (6 mm, i.d.) at atmospheric pressure. In each test, 0.3 g of the catalyst (40–60 mesh) was placed into the tube reactor. Prior to testing, the catalysts were pretreated at 200 °C with N<sub>2</sub> for 1 h. The MEK feed (800 ppm) was generated by using a N<sub>2</sub> bubbler in thermostatic bath at 35 °C and mixing with air (79% N<sub>2</sub> + 21% O<sub>2</sub>). The total flow rate was kept at 212 mL·min<sup>-1</sup> (space velocity of 42600 mL·g<sup>-1</sup>·h<sup>-1</sup>). The concentrations of MEK, CO and CO<sub>2</sub> were measured by an online gas chromatography (GC-9890B; Shanghai Linghua Co., China) equipped with a flame ionization detector (FID) and HT-Wax column in 30 m × 0.32 mm (ID) × 0.5 μm. The conversion of MEK (*X*<sub>MEK</sub>) was calculated as Eq. (1),

$$X_{\text{MEK}}(\%) = \frac{[\text{MEK}]_{\text{in}} - [\text{MEK}]_{\text{out}}}{[\text{MEK}]_{\text{in}}} \times 100\% \quad (1)$$

where  $[\text{MEK}]_{\text{in}}$  and  $[\text{MEK}]_{\text{out}}$  represent the MEK concentrations in the inlet and outlet gas, respectively.

CO<sub>2</sub> selectivity (*S*<sub>CO<sub>2</sub></sub>) was calculated as Eq. (2),

$$S_{\text{CO}_2}(\%) = \frac{[\text{CO}_2]_{\text{out}}}{4 \times [\text{MEK}]_{\text{in}} \times X_{\text{MEK}}} \times 100\% \quad (2)$$

where  $[\text{CO}_2]_{\text{out}}$  is the CO<sub>2</sub> concentrations in the outlet gas.

Stability test was carried out at 220 °C for 10 h after a heating processing for MEK combustion, followed by a cooling processing. Recycle experiment was carried out at the same conditions as activity evaluation. After the MEK oxidation finished at 190 °C, the catalyst was left in the reactor and the heating was suspended. When reactor was cool down to room temperature, another oxidation cycle was started by repeating the same heating procedure. The recycle experiment was carried out for three cycles. For consideration of the water vapor's effect on the catalytic activity, the on-stream MEK oxidation experiments were carried out in the presence and absence of 3 vol.% and 1 vol.% water vapor, which were introduced by automatic sample injector through pretreatment processor at 100 °C.

The reaction rate ( $r_{\text{MEK}}$ ,  $\text{mol} \cdot \text{g}_{\text{Pt}}^{-1} \cdot \text{s}^{-1}$ ) was calculated as Eq. (3),

$$r_{\text{MEK}} = \frac{X_{\text{MEK}} \cdot V_{\text{MEK}}}{W_{\text{cat}} \cdot w\%_{\text{Pt}}} \quad (3)$$

where  $W_{\text{cat}}$  represents the catalyst weight (g),  $w\%_{\text{Pt}}$  is the content of Pt in catalyst (%),  $V_{\text{MEK}}$  is the MEK gas flow rate ( $\text{mol} \cdot \text{s}^{-1}$ ).

When the conversion of MEK is < 15%, a dependence of the reaction rate ( $r_{\text{MEK}}$ ) on the products of  $\text{CO}_2$  and  $\text{H}_2\text{O}$  may be ignored, and the empirical kinetic expression of the reaction rate equation of MEK oxidation can be described as Eq. (4),

$$r_{\text{MEK}} = A \exp\left(-\frac{E_a}{RT}\right) P_{\text{MEK}}^\alpha P_{\text{O}_2}^\beta \quad (4)$$

Taking the natural logarithm of Eq. (4), Eq. (5) can be obtained.

$$\ln r = \ln A + \alpha \ln P_{\text{MEK}} + \beta \ln P_{\text{O}_2} - E_a/(RT) \quad (5)$$

The components of the reactant feed gas undergo minor changes during the kinetics data testing, and the conversion of MEK is < 15%. Therefore,  $\ln A$ ,  $\alpha \ln P_{\text{MEK}}$  and  $\beta \ln P_{\text{O}_2}$  can be supposed to be approximately constant, and Eq. (5) can be simplified to Eq. (6),

$$\ln r = -\frac{E_a}{RT} + C \quad (6)$$

The activation energy ( $E_a$ ) can be obtained from the slope of the resulting linear plot of  $\ln r$  versus  $1/T$ .

The turnover frequency based on the Pt nanoparticles ( $\text{TOF}_{\text{Pt}}$ ,  $\text{s}^{-1}$ ) was calculated as Eq. (7),

$$\text{TOF}_{\text{Pt}} = \frac{X_{\text{MEK}} \cdot V_{\text{MEK}} \cdot N_A}{W_{\text{cat}} \cdot w\%_{\text{Pt}} \cdot D_{\text{Pt}}} \quad (7)$$

where  $N_A$  is the Avogadro constant,  $D_{\text{Pt}}$  represents the dispersion of Pt nanoparticles on catalysts (%).

### 3. Results

#### 3.1. Structural characteristics

##### 3.1.1. XRD

According to small-angle XRD (Fig. 1A), a relatively sharp peak at  $1.6\text{--}3.0^\circ$  along with other two weak peaks at  $4.2^\circ$  and  $4.8^\circ$  for NRS are ascribed to the (100), (110) and (200) reflections of materials with 2D-hexagonal ( $p6mm$ ) symmetry, confirming the highly ordered mesostructured of NRS [22], in consistent with  $\text{N}_2$  sorption results (Fig. S3). However, the pattern of KA-NRS only displays a basal diffraction peak of lower intensity and poorly discernible higher order peaks, corresponding to a less ordered mesoporous structure, which indicates that the aluminated grafting method affects the original mesostructure of the synthesized catalysts [23], in line with the BET analysis (Table 1). Additionally, no small-angle diffraction peaks were observed over SNFS and KA-SNFS, suggesting that these samples possess an irregular pore structure [23]. Wide-angle XRD (Fig. 1B) shows that all catalysts exhibit a diffraction peak at  $2\theta = 23^\circ$ , which can be ascribed to the amorphous silica. Three diffraction peaks at  $2\theta = 39.7^\circ$ ,  $46.3^\circ$  and  $67.5^\circ$  observed in diffraction patterns of 0.39 wt.% Pt/KA-NRS and 0.45 wt.% Pt/KA-SNFS are assigned to the (111), (200) and (220) planes of metallic Pt, respectively [24]. These peaks become weaker and broader with decreasing Pt content due to the low loading and improved dispersion [10]. As shown in Table 1, the dispersion of Pt nanoparticles over 0.39 wt.% Pt/KA-NRS sample is 45.3%, which increases to 74.9% over 0.01 wt.% Pt/KA-NRS. The characteristic peak of  $\text{Al}_2\text{O}_3$  at  $2\theta = 44.6^\circ$  ascribing to the process of aluminization [25] can be observed in all catalysts except 0.14 wt.% Pt/MCM-41.

##### 3.1.2. FE-SEM and HR-TEM

Fig. 2 shows the FE-SEM and HR-TEM images of typical samples. From Fig. 2A and B, the KA-SNFS support presents uniform particle size

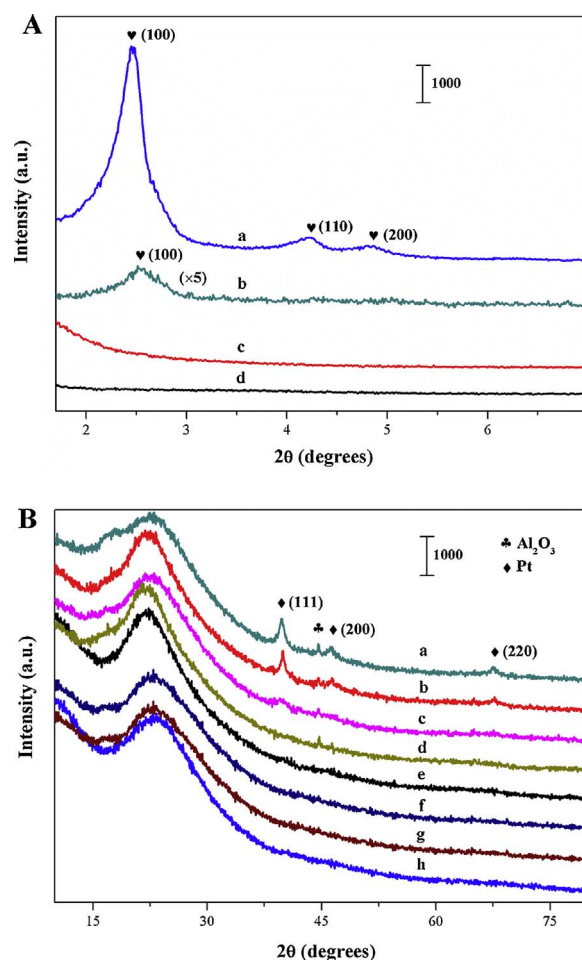


Fig. 1. (A) Small-angle XRD patterns of (a) NRS, (b) KA-NRS, (c) SNFS and (d) KA-SNFS; (B) Wide-angle XRD patterns of (a) 0.39 wt.% Pt/KA-NRS, (b) 0.45 wt.% Pt/KA-SNFS, (c) 0.27 wt.% Pt/KA-NRS, (d) 0.1 wt.% Pt/KA-NRS, (e) 0.07 wt.% Pt/KA-SNFS, (f) 0.04 wt.% Pt/KA-NRS, (g) 0.01 wt.% Pt/KA-NRS and (h) 0.14 wt.% Pt/MCM-41.

and a flower-like spherical morphology with wrinkled radial structure ranging from 150 to 410 nm. The thickness of the radial wrinkled “petal” structure is *ca.* 10 nm. From Fig. 2C and D, the KA-NRS support takes on the shape of irregular curving nano-rod, the length and width ranging from 800 nm to 1.9  $\mu\text{m}$  and 100 nm to 250 nm, respectively. The HR-TEM image of KA-SNFS support (Fig. 2E) shows a great number of hierarchical pores distributed on the nano-flowers with a dandelion-like shape, including worm-like mesopores, micropores and cone-shaped macropores, formed by overlapping areas in the wrinkled radial structure. The HR-TEM image of KA-NRS support (Fig. 2F) shows that the curving nano-rod silica is rough and hold the comparable lengths.

From Fig. 2G, NRS possesses a surface lattice spacing of 2.063 nm for the (100) crystal planes, which confirmed by the small-angle XRD (Fig. 1A). From Fig. 2H and I, the average size of Pt nanoparticles over 0.45 wt.% Pt/KA-SNFS and 0.39 wt.% Pt/KA-NRS are found to be  $4.5 \pm 2$  nm and  $2.6 \pm 0.7$  nm, respectively, indicating an uniform distribution of Pt particles with a very narrow range over the catalysts. The Pt nanoparticles on 0.39 wt.% Pt/KA-NRS are highly dispersed. However, the Pt nanoparticles aggregate to some extent when supported on KA-SNFS. The larger particle size leads to low dispersion of Pt nanoparticles over 0.45 wt.% Pt/KA-SNFS (5.4%) compared with 0.39 wt.% Pt/KA-NRS (54.3%) (Table 1), which can be ascribed to the large specific surface area and micropore volume and uniform pore structure of NRS supports. Fig. 2J and K show three different lattice planes with spacing of 0.1202, 0.072, and 0.0937 nm, which separately correspond to the (111), (220) and (200) planes of metallic Pt,

**Table 1**  
Textural property of all synthesized catalysts.

Sample	Pt content <sup>a</sup> (wt.%)	Dispersion <sup>b</sup> (%)	$S_{\text{BET}}$ <sup>c</sup> ( $\text{m}^2\cdot\text{g}^{-1}$ )	$V_{\text{pore}}$ <sup>d</sup> ( $\text{cm}^3\cdot\text{g}^{-1}$ )	$V_{\text{micro}}$ <sup>e</sup> ( $\text{cm}^3\cdot\text{g}^{-1}$ )	$d_{\text{pore}}$ <sup>f</sup> (nm)
NRS	/	/	942.4	0.73	0.38	3.5
SNFS	/	/	199.1	0.89	0.09	19.3
0.39 wt.% Pt/KA-NRS	0.50 (0.39)	45.3	596.6	0.52	0.26	3.8
0.27 wt.% Pt/KA-NRS	0.30 (0.27)	67.0	650.8	0.64	0.27	4.9
0.1 wt.% Pt/KA-NRS	0.10 (0.10)	69.0	662.8	0.56	0.27	3.8
0.04 wt.% Pt/KA-NRS	0.05 (0.04)	64.7	561.7	0.56	0.25	4.3
0.01 wt.% Pt/KA-NRS	0.01 (0.01)	74.9	627.5	0.54	0.26	4.2
0.45 wt.% Pt/KA-SNFS	0.50 (0.45)	5.4	139.9	0.56	0.07	14.8
0.07 wt.% Pt/KA-SNFS	0.10 (0.07)	22.2	117.8	0.43	0.06	13.1
0.14 wt.% Pt/MCM-41	0.50 (0.14)	23.6	1138.8	1.16	0.49	3.4
0.15 wt.% Pt/ $\gamma$ - $\text{Al}_2\text{O}_3$	0.50 (0.15)	29.1	327.2	0.47	0.14	4.6

<sup>a</sup> Nominal Pt content and actual Pt content (in the parenthesis) detected by ICP-OES.

<sup>b</sup> Dispersion of Pt estimated by HOT.

<sup>c</sup> Specific surface area obtained at  $P/P_0 = 0.05$ – $0.30$ .

<sup>d</sup> Total pore volume estimated at  $P/P_0 = 0.99$ .

<sup>e</sup> Micropore volume estimated from the  $t$ -plot method.

<sup>f</sup> BJH pore diameter calculated from the desorption branch.

indicating the formation of active sites with well-defined crystallinity. Furthermore, the EDS mapping images of O, Al, Pt elements over 0.39 wt.% Pt/KA-NRS sample are shown in Fig. 2L–N. A uniform distribution of O, Al and Pt in the particle region and the related peaks can be seen clearly, confirming the homogeneous Pt nanoparticles distribution over the surface of KA-NRS support. The STEM-EDX and HAADF-STEM (insert) further confirmed that Pt nanoparticles are homogeneously dispersed over the surface of KA-NRS support (Fig. 2O). In addition, the Pt content measured by EDX (0.48 wt.%) is similar to the results obtained by ICP-OES (Table 1).

### 3.1.3. Dispersion and content of active sites

From Table 1, the actual content of Pt measured by ICP-OES is similar to the theoretical preparatory content when supported on KA-NRS and KA-SNFS demonstrating that the ethylene glycol reduction and colloid impregnation methods are efficient for preparing supported noble metal catalysts. On the contrary, it is inefficient for MCM-41 and  $\gamma$ - $\text{Al}_2\text{O}_3$  to support noble metals through wetness impregnation (WI). Furthermore, it is difficult to control the particle size and active sites for the conventional wetness impregnation method. In this work, the dispersion of Pt nanoparticles characterized by hydrogen and oxygen titration (HOT) shows that the Pt dispersion decreases with an increasing of Pt content and determined by the property of support as well (Table 1). The dispersion of Pt nanoparticles over 0.39 wt.% Pt/KA-NRS sample is 45.3%, which rises up to 74.9% over 0.01 wt.% Pt/KA-NRS. The Pt nanoparticles are nearly monodisperse over the 0.01 wt.% Pt/KA-NRS catalyst. For the 0.14 wt.% Pt/MCM-41 catalyst, the Pt dispersion is 23.6%, which consistent with the previously reported results (Wang et al. [26]. prepared 0.45 wt.% Pt/ZSM-22 with 31.48% dispersion and Zhu et al. [10]. synthesized 1.0 wt.% Pt/SBA-15 with 24.6% by the wetness impregnation method). The basis of results attribute to the acid sites of the support and preparation method.

## 3.2. Textural properties

### 3.2.1. FT-IR and ESR

Fig. 3A shows the FT-IR results of all synthesized catalysts. All samples exhibit a broad and intensive absorption peak at around  $3447\text{ cm}^{-1}$ , which is attributed to the stretching and bending vibrations of surface hydroxyls and/or adsorbed water molecules. The surface hydroxyls also give rise to a band of  $\delta(\text{Si-OH})$  and  $\nu(\text{Si-OH})$  at  $1642\text{ cm}^{-1}$  [27]. Compared with Pt/MCM-41, the peak of  $\delta(\text{Si-OH})$  and  $\nu(\text{Si-OH})$  over Pt/KA-NRS and Pt/KA-SNFS samples are strengthened obviously, ascribed to the addition of Al atoms. A sharp peak at  $574\text{ cm}^{-1}$  can be assigned to the vibration mode of  $\text{AlO}_6$ , which

indicates that the Al atom has been incorporated into the framework of the silica. The peak at  $800\text{ cm}^{-1}$  in all spectra is ascribed to the typical symmetric stretching vibration of the O-Si-O bond of mesoporous silica, and the peak at  $458\text{ cm}^{-1}$  can be ascribed to symmetric bending vibrations of tetrahedral Si-O of silica [28].

The electron spin resonance (ESR) spectroscopy, measured at 293 K was used to study the conduction electron spin resonance (CESR) of small platinum particles. This method was successfully applied to platinum loaded on silica, zeolites or alumina. From Fig. 3B, the spectrum signal at  $g = 2.141$  mT detected in all samples are the defect centers induced in the aluminosilica framework, which are potential sites for adsorbed oxygen and incorporated metallic Pt atoms [29]. Furthermore, a similarly broad ESR signal at  $g = 2.239$  mT corresponds to the spectrum of metallic Pt for 0.39 wt.% Pt/KA-NRS and 0.45 wt.% Pt/KA-SNFS catalysts [30], which is faint over 0.27 wt.% Pt/KA-NRS sample attributing to the low content and higher dispersion (67%) of Pt nanoparticles. The Pt signal can be attributed to nano-crystalline Pt with a particle size of *ca.* 2.7 nm, in good agreement with the results of HR-TEM (Fig. 2I) [31]. From the same  $g$  tensor it can be concluded that the Pt atom coordination is comparable in these two samples.

### 3.2.2. UV-vis and raman

The ultraviolet-visible spectroscopy (UV-vis) can give information for metals of very small primary particle size ( $< 4\text{ nm}$ ), and low content ( $< 1\text{ wt.}\%$ ) [32], where the XRD method is unsuccessful. From Fig. 3C, for KA-NRS and KA-SFNS support, the band at around 241.8 nm was assigned to Al-O charge-transfer transition of four-coordinated framework, which refers to structures with highly ordered octahedral symmetry and stabilized in the framework of silica [33]. This band shifts toward high energy of 257.2 nm after loading Pt nanoparticles due to Al-O-Pt [34]. For 0.39 wt.% Pt/KA-NRS, 0.1 wt.% Pt/KA-NRS, 0.45 wt.% Pt/KA-SFNS and 0.07 wt.% Pt/KA-SFNS, the presence of the band centered at 294.7 nm is the characteristic absorbance of Pt particles for metal-support interaction [35]. According to previous reports, the absorption band in the 400–500 nm range corresponds to  $\text{Pt}^{4+}$  [36], whereas that in the 600–800 nm range to  $\text{Pt}^{2+}$  [37], but neither of them were detected in this work, which indicates that the Pt nanoparticles exist in metallic  $\text{Pt}^0$  over samples.

Fig. 3D depicts Raman shift spectra for as-prepared samples in the range  $300$ – $1200\text{ cm}^{-1}$ . Compared with 0.45 wt.% Pt/KA-SFNS and 0.39 wt.% Pt/KA-NRS catalysts, oxidized 0.45 wt.% Pt/KA-SFNS, oxidized 0.39 wt.% Pt/KA-NRS and 0.14 wt.% Pt/MCM-41 samples display the signals at  $689\text{ cm}^{-1}$ , which can be ascribed to Pt-O vibration [38]. However, this single is not detected in the case of 0.45 wt.% Pt/KA-SFNS and 0.39 wt.% Pt/KA-NRS catalysts, indicating that the active



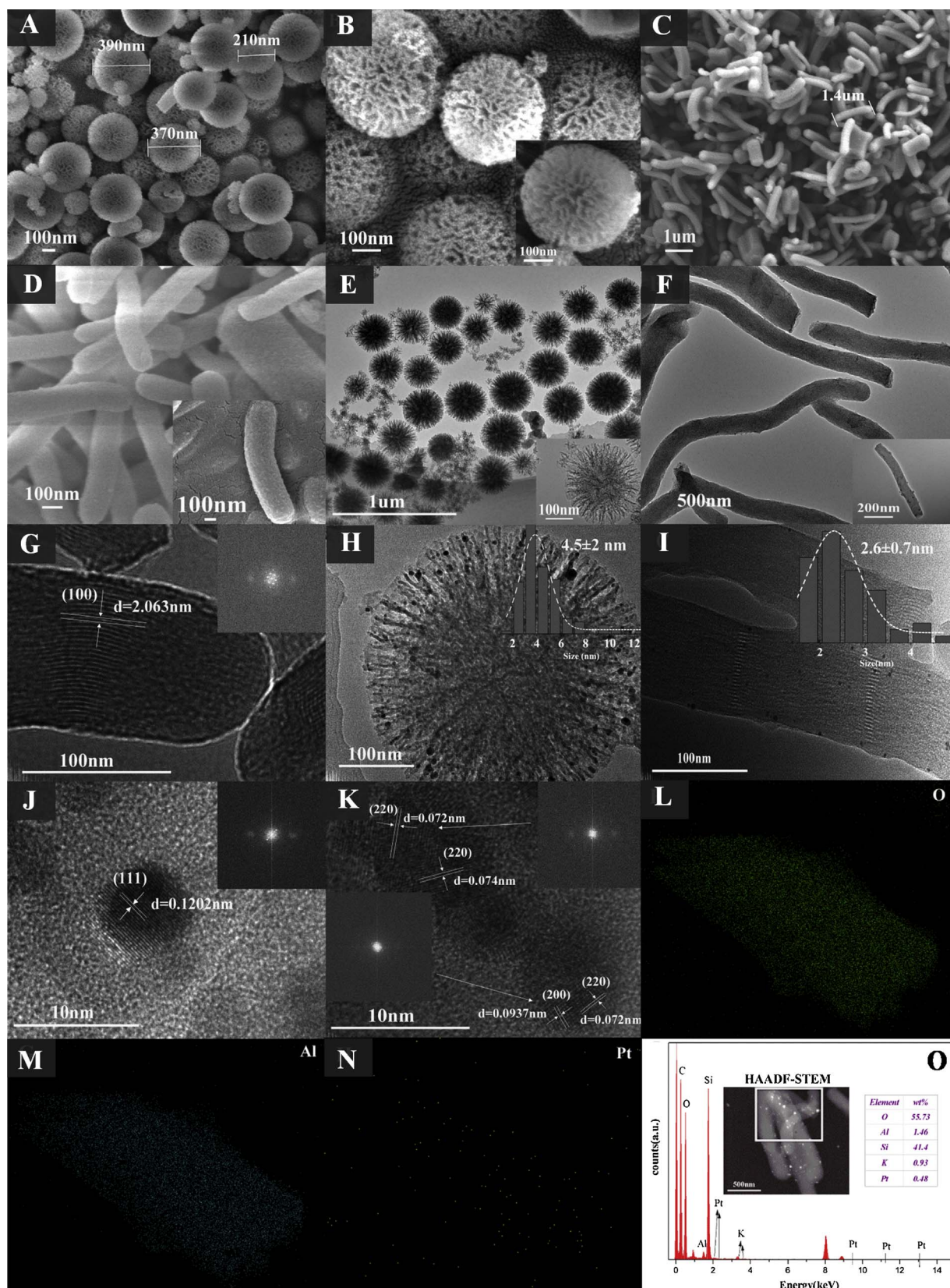


Fig. 2. FE-SEM images of (A,B) KA-SNFS and (C,D) KA-NRS; HR-TEM images of (E) KA-SNFS, (F,G) KA-NRS, (H) 0.45 wt.% Pt/K-SNFS and (I-K) 0.39 wt.% Pt/K-SNFS; EDS mapping images of (L-N) 0.39 wt.% Pt/K-SNFS; STEM-EDX and HAADF-STEM (insert) images of (O) 0.39 wt.% Pt/K-SNFS.





metallic form. Considering that O 1s signals may originate from different oxygen environments, O 1s spectra were deconvoluted into three peaks according to previous work [39]. Three divided peaks of 0.45 wt.% Pt/K A-SNFS at about 533.6 eV, 532.8 eV and 532.1 eV are respectively assigned to binding energies of oxygen associated to Si-OH (silanol group), Si-O-Si and AlO (aluminate anion compensated by potassium cation), and of 0.39 wt.% Pt/K A-NRS at about 533.5 eV, 532.9 eV and 532.2 eV, respectively. The peak of Si-OH is mainly ascribed to the surface hydroxyl and absorbed water present. The peaks shift towards high binding energy with decreasing of Pt content. Fig. 4C shows the K 2p XPS spectra of samples. K elements were doped by an ion-exchanged method, which promote the catalytic activity of noble metal based catalysts [12]. K addition leads to the formation of a well-dispersed Pt species that facilitate the activation of surface OH groups and chemisorbed oxygen [40]. The fitting analysis of these spectra reveals that they are formed by two different forms of potassium. The main peak at the binding energy range of 294.1–294.5 eV is K  $2p_{3/2}$  corresponding to  $K^+$ , which is assigned to the AlO (aluminate anion compensated by potassium cation) and to surface K [41]. Otherwise, the small shoulder peak at the binding energy range 296.8–297.3 eV is ascribed to  $K^0$  (K  $2p_{1/2}$ ) through coordination with  $Pt^0$  [42]. The molar ratio of K  $2p_{3/2}$ /K  $2p_{1/2}$  on the surface of 0.37 wt.% Pt/K A-NRS and 0.45 wt.% Pt/K A-SNFS are approximately 2.75 and 2.95, respectively (Table S2), which represents the ratio of  $K^+/K^0$ . The low ratio of K  $2p_{3/2}$ /K  $2p_{1/2}$  indicates that more K atoms exist as  $K^0$  coordinated with  $Pt^0$ . Furthermore, the ratio of K  $2p_{3/2}$ /K  $2p_{1/2}$  increases with the decreasing of Pt content, ascribed to the reduction of  $K^0$  content (coordinating with  $Pt^0$ ). It further demonstrates that Pt nanoparticles were coordinated with  $K^0$ . As shown in Fig. 4D, since the Al 2p peak strongly overlaps with Pt 4f peak of the active phase in the range of 81–66 eV, it is necessary to separate the Al 2p peak from these spectra. The decomposition of the spectra to individual components of Al 2p at binding energy of 75.1–75.5 eV for active samples in the present study [43]. The deconvoluted peak area of Al 2p for Pt/K A-SNFS samples is larger than that from the Pt/K A-NRS samples and signifies a higher relative content of Al over the catalysts. Al atoms are incorporated with silanol groups, therefore, the higher Al content means a lower silanol population, which impacts the adsorption of MEK and the stability of catalysts. The XPS profiles for Pt are divided into two strong peaks. The peak component with binding energy around 71.2–71.5 eV is Pt  $4f_{7/2}$  (represents  $Pt^0$  connected with K), and around 74.4–74.8 eV is Pt  $4f_{5/2}$  (represents  $Pt^0$  on the surface of support alone) [44]. Both of these two peaks are assigned to the  $Pt^0$  state [45]. No peak of  $Pt^{2+}$  and  $Pt^{4+}$  is found in spectra, indicating Pt nanoparticles exist as metallic Pt, which is also confirmed by O 1s (Fig. 4B). The peak of Pt  $4f_{7/2}$  becomes insignificant with decreasing of Pt content. The ratio of Pt  $4f_{7/2}$ /Pt  $4f_{5/2}$  is approximately 1.83, 1.23, and 0.84 for 0.37 wt.% Pt/K A-NRS, 0.37 wt.% Pt/K A-SNFS, and 0.45 wt.% Pt/K A-SNFS, respectively, and the sequence for all samples is: 0.37 wt.% Pt/K A-NRS (1.83) > 0.37 wt.% Pt/K A-SNFS (1.23) > 0.45 wt.% Pt/K A-SNFS (0.84) > 0.10 wt.% Pt/K A-NRS (0.33) > 0.07 wt.% Pt/K A-SNFS (0.12) > 0.01 wt.% Pt/K A-NRS (0.02). A higher ratio of Pt  $4f_{7/2}$ /Pt  $4f_{5/2}$  represents more metallic Pt nanoparticles connecting with K atoms to form  $Pt^0$ , which are active sites for catalytic oxidation reaction. Therefore,  $H_2$  reduction for catalysts is desirable for enhancing the catalytic activity; which is consistent with results reported previously [13].

### 3.3. FT-IR spectra for $NH_3$ and CO adsorption

#### 3.3.1. FT-IR spectra for $NH_3$ adsorption

The acidity of support, fresh and used catalysts is evaluated via  $NH_3$ -IR (Fig. 5A). There are no characteristic peaks of  $NH_3$  adsorption for NRS support. For fresh 0.27 wt.% Pt/K A-NRS catalyst, the bands in the range of 1298–1431  $cm^{-1}$  could be attributed to the asymmetric and symmetric bending vibrations of  $NH_4^{+}$  species on the Brønsted acidic sites [46]. Meanwhile, the incorporation of Al species would be likely to

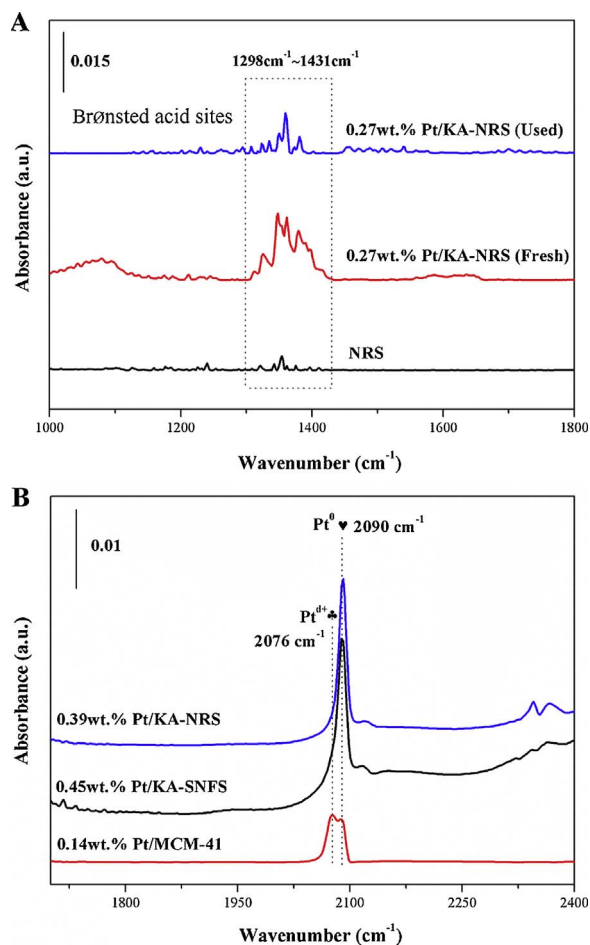


Fig. 5. (A) FT-IR spectra for  $NH_3$  adsorption of catalysts; (B) FT-IR spectra for CO adsorption of catalysts.

generate Brønsted acids and enhance the total acidity of the sample. Compared with fresh catalyst, the intensity of characteristic peak become weak for used 0.27 wt.% Pt/K A-NRS, ascribed to the adsorption of MEK over catalysts and provide proton for producing intermediate products. Furthermore, compared with the traditional wetness impregnation method, ethylene glycol reduction and colloid impregnation methods are able to control particle size and prevent sintering of Pt nanoparticles, which are important for improving active sites dispersion [47]. The dispersion of noble metal over catalysts has a significant effect on catalytic activity [12], that is, higher dispersion intends to create more active sites and promote the catalytic efficiency. In this work, the 0.27 wt.% Pt/K A-NRS catalyst possess outstanding catalytic activity for MEK combustion with a dispersion of 67.0%. The dispersion of active sites achieve 74.9% over 0.01 wt.% Pt/K A-NRS catalyst. Highly dispersed active sites maintain considerable activity even with low content of Pt nanoparticles.

#### 3.3.2. FT-IR spectra for CO adsorption

A large proportion of metallic  $Pt^0$  is an important factor for VOC combustion. The  $Pt^0$  active sites are more beneficial for MEK combustion than  $Pt^{2+}$  and  $Pt^{4+}$  [13]. In this work, the metallic Pt nanoparticles are produced through ethylene glycol reduction and  $H_2$  reduction methods, which has been confirmed by wide-angle XRD (Fig. 1B), UV-vis (Fig. 3C), Raman (Fig. 3D), XPS (Fig. 4) and  $H_2$ -TPR (Fig. S4A). In this work, CO was used as a probe molecule to investigate the active sites on the catalysts due to the utility of CO in FT-IR spectroscopy, which can provide information related to the active sites of an adsorbed species and to the chemical environment of Pt nanoparticles [48].

When CO adsorbs on Pt active sites, the electrons are partially transferred from a  $d$ -orbital of the metal to the anti-bonding CO molecular orbital. This electron-transfer strengthens the Pt–C bond and weakens the C–O bond. The strengthening of the Pt–CO bond is reflected in the increasing of the vibrational frequencies for the Pt–C bond [49].

As shown in Fig. 5B, for 0.39 wt.% Pt/KA-NRS and 0.45 wt.% Pt/KA-SNFS, the band appears at  $2090\text{ cm}^{-1}$  is assigned to linear CO adsorbed on different terrace and step sites of metallic platinum crystallites ( $\text{Pt}^0$ ) [50]. This band is the characteristic peak of CO adsorbed on Pt (111) planes based on its shape and intensity [51], which verifies that the Pt (111) planes are dominating exposed planes for monodispersed Pt active sites in this work, and make a significant contribution to MEK combustion. The results are confirmed by wide-angle XRD (Fig. 1B). In contrast, two wide peaks emerge into 0.14 wt.% Pt/MCM-41 sample for CO adsorption. The band at  $2090\text{ cm}^{-1}$  is the linear CO adsorbed on  $\text{Pt}^0$ , however, the band at around  $2076\text{ cm}^{-1}$ , which is assigned to bridge-type CO adsorbed on large platinum crystallites or correspond to adsorption on oxidized  $\text{Pt}^{2+}/\text{Pt}^{4+}$  atoms [52].

FT-IR characterization by the means of CO probe technique is sensitive to the particle size and metal support interactions, since it is affected by the electronic properties of Pt surface atoms. According to the peaks of FT-IR for CO adsorption on 0.39 wt.% Pt/KA-NRS, 0.45 wt.% Pt/KA-SNFS and 0.14 wt.% Pt/MCM-41 samples, the particle size of Pt nanoparticles can be identified as *ca.* 2, 3 and 10 nm, respectively, according to the position and shape of the characteristic peak of CO adsorption [53], which are corresponding to the results of HR-TEM (Fig. 2H and I). Furthermore, the band width of the FT-IR peak for 0.39 wt.% Pt/KA-NRS and 0.45 wt.% Pt/KA-SNFS was narrower than that for 0.14 wt.% Pt/MCM-41, implying that uniform, small Pt particles were likely formed over the 0.39 wt.% Pt/KA-NRS and 0.45 wt.% Pt/KA-SNFS samples [48]. Compared with traditional Pt/MCM-41 catalyst, a larger proportion of metallic Pt and highly dispersed Pt with smaller particle size contribute to efficient combustion of MEK for Pt/KA-NRS and Pt/KA-SNFS samples.

### 3.4. Catalytic performance

#### 3.4.1. MEK oxidation activity

The catalytic behaviors of MEK oxidation were studied, as shown in Fig. 6. In addition, the specific reaction data (temperatures at which 5%, 50% and 90% conversion of MEK, reaction rate, apparent activation energy and turnover frequency) of all synthesized catalysts were also calculated and listed in Table 2. The factors of Mears criterion ( $N_M$ ) and the Weisz-Prater criterion ( $N_{W-P}$ ) were calculated and evaluated at  $T_{100}$ ,  $T_{50}$ , and  $T_{10}$  (the temperature at which the corresponding MEK conversion was achieved) to estimate the influence of external and internal diffusion effects on the reaction rates [54]. The calculated values at  $T_{100}$ ,  $T_{50}$ , and  $T_{10}$  show that  $N_M < 0.15$  and  $N_{W-P} < 0.3$  for all the catalysts, indicating that both the external and the internal diffusion effects on the catalytic performance can be ignored [54]. We consider that operation under MEK-lean conditions, with a thin catalyst bed, large specific surface area, uniform pore structures and well-proportioned particle sizes, the effect of heat transfer can also be ignored.

Fig. 6A shows the catalytic activity of MEK combustion over synthesized catalysts. The KA-NRS and KA-SNFS support show negligible activity even at  $300^\circ\text{C}$ , which indicates that the addition of Pt evidently improves the catalytic performance at low temperature. The 0.39 wt.% Pt/KA-NRS and 0.45 wt.% Pt/KA-SNFS respectively gives 100% and 92% conversions of MEK at  $190^\circ\text{C}$ , while for 0.14 wt.% Pt/MCM-41 and 0.15 wt.% Pt/ $\gamma\text{-Al}_2\text{O}_3$ , only achieve *ca.* 20% and 17% respectively under this temperature. Therefore, supported Pt nanoparticles on KA-NRS and KA-SNFS are more efficient compared to the conventional MCM-41 and  $\gamma\text{-Al}_2\text{O}_3$  supports. In order to investigate the effect of Pt content, 0.1 wt.% Pt/KA-NRS and 0.07 wt.% Pt/KA-SNFS were also prepared. As the results shown in Fig. 6A, 0.1 wt.% Pt/KA-NRS ( $T_{90}$  of  $208^\circ\text{C}$ ) is modestly more active than 0.07 wt.% Pt/KA-SNFS ( $T_{90}$  of

$216^\circ\text{C}$ ). Above results indicate that the Pt/KA-NRS catalyst is the preferable catalyst to Pt/KA-SNFS regardless of Pt content, which can be explained by the difference in the textural and structural properties of these catalysts. In comparison with KA-SNFS, KA-NRS possesses a larger specific surface area and micropore volume and uniform pore structure. Besides, the Pt nanoparticles on KA-NRS are nearly monodisperse, which offers more active sites. Monodisperse Pt nanoparticles supported on KA-NRS show outstanding catalytic activity in MEK catalytic oxidation at low temperature.

Fig. 6B shows the oxidation of MEK over Pt/KA-NRS catalysts with different Pt loadings, and the activity of various samples decrease in the sequence of 0.27 wt.% Pt/KA-NRS > 0.29 wt.% Pt/KA-NRS > 0.1 wt.% Pt/KA-NRS > 0.01 wt.% Pt/KA-NRS > 0.04 wt.% Pt/KA-NRS. The 0.27 wt.% Pt/KA-NRS catalyst possesses the highest activity with 5%, 50%, and 90% of MEK converted at only  $95^\circ\text{C}$ ,  $144^\circ\text{C}$ , and  $163^\circ\text{C}$ , respectively. The catalytic activity not only associates with Pt content, but also correlates to surface area of supports and dispersion of active sites. The 0.27 wt.% Pt/KA-NRS catalyst holds the high dispersion of active sites (67.0%) and larger specific surface area of support ( $650\text{ m}^2/\text{g}$ ) than 0.39 wt.% Pt/KA-NRS (45.3% of dispersion and  $596\text{ m}^2/\text{g}$  of specific surface area), which leads to a superior activity although the lower Pt content of 0.27 wt.% Pt/KA-NRS catalyst compared to 0.39 wt.% Pt/KA-NRS. As shown in Table S1, the 0.27 wt.% Pt/KA-NRS catalyst achieves more than  $100^\circ\text{C}$  temperature reduction compared to some typical catalysts (Pd/ $\text{Al}_2\text{O}_3$ , Pt/BASap, and Pd/ZSM-5) with superior performances for MEK oxidation even under much higher GHSV.

High  $\text{CO}_2$  selectivity represents an important parameter for catalytic oxidation of VOCs. Accordingly,  $\text{CO}_2$  selectivity of three most active catalysts (0.27 wt.% Pt/KA-NRS, 0.39 wt.% Pt/KA-NRS, and 0.45 wt.% Pt/KA-SNFS) were further studied, as shown in Fig. 6C. The  $\text{CO}_2$  selectivity of these catalysts are in order of 0.27 wt.% Pt/KA-NRS ( $190^\circ\text{C}$  of 100%) > 0.39 wt.% Pt/KA-NRS ( $212^\circ\text{C}$  of 100%) > 0.45 wt.% Pt/KA-SNFS ( $220^\circ\text{C}$  of 100%), which is in accordance with that of the MEK conversion results in Fig. 6A and B. Typically, the  $\text{CO}_2$  selectivity of 0.27 wt.% Pt/KA-NRS catalyst is as high as 96% at  $150^\circ\text{C}$  and reaches 100% at  $190^\circ\text{C}$ , which is much higher than that of 0.45 wt.% Pt/KA-SNFS (68% at  $150^\circ\text{C}$  and 91% at  $190^\circ\text{C}$ ) although it shows very high activity for MEK oxidation. These results further demonstrate that a 0.27 wt.% Pt/KA-NRS catalyst is a very powerful and promising catalyst for complete oxidation of MEK. However, there is an abnormal region (Fig. 6C) for all the studied catalysts with respect to the  $\text{CO}_2$  selectivity (the value presents a parabola shape with the increasing of temperature) in different temperature ranges ( $149\text{--}160^\circ\text{C}$  for 0.27 wt.% Pt/KA-NRS,  $159\text{--}169^\circ\text{C}$  for 0.39 wt.% Pt/KA-NRS, and  $170\text{--}199^\circ\text{C}$  for 0.45 wt.% Pt/KA-SNFS), and the reason for this phenomenon will be discussed in the following part.

#### 3.4.2. Stability and effect of water vapor

The stability is an important property for supported noble metal catalysts. As shown in Fig. 6D, insignificant loss in catalytic activity was observed for active catalysts (0.27 wt.% Pt/KA-NRS, 0.39 wt.% Pt/KA-NRS, and 0.45 wt.% Pt/KA-SNFS) at  $220^\circ\text{C}$  for 10 h of on-stream reaction at a GHSV of  $42,600\text{ mL}\cdot\text{g}^{-1}\cdot\text{h}^{-1}$  between heating and cooling processes, demonstrating that these samples possess excellent stability in the complete oxidation of MEK. Fig. 6E shows the circulation of heating and cooling process for MEK combustion over 0.27 wt.% Pt/KA-NRS. The performance of MEK combustion is stable during three times circulation, which illustrates that the heating and cooling processes have a negligible impact on 0.27 wt.% Pt/KA-NRS catalyst.

As moisture is one of the reaction products, it is important to evaluate its effect on catalytic behavior, particularly in terms of stability. Fig. 6F illustrates the influence of water vapor on the catalytic performance when introducing 3 vol.% and 1 vol.% water vapor into the feed stream at  $180^\circ\text{C}$ . It is found that only about *ca.* 4.5% and 10.3% loss in MEK conversion for 0.27 wt.% Pt/KA-NRS and 0.39 wt.% Pt/KA-NRS catalyst when 3 vol.% water vapor was introduced, while the



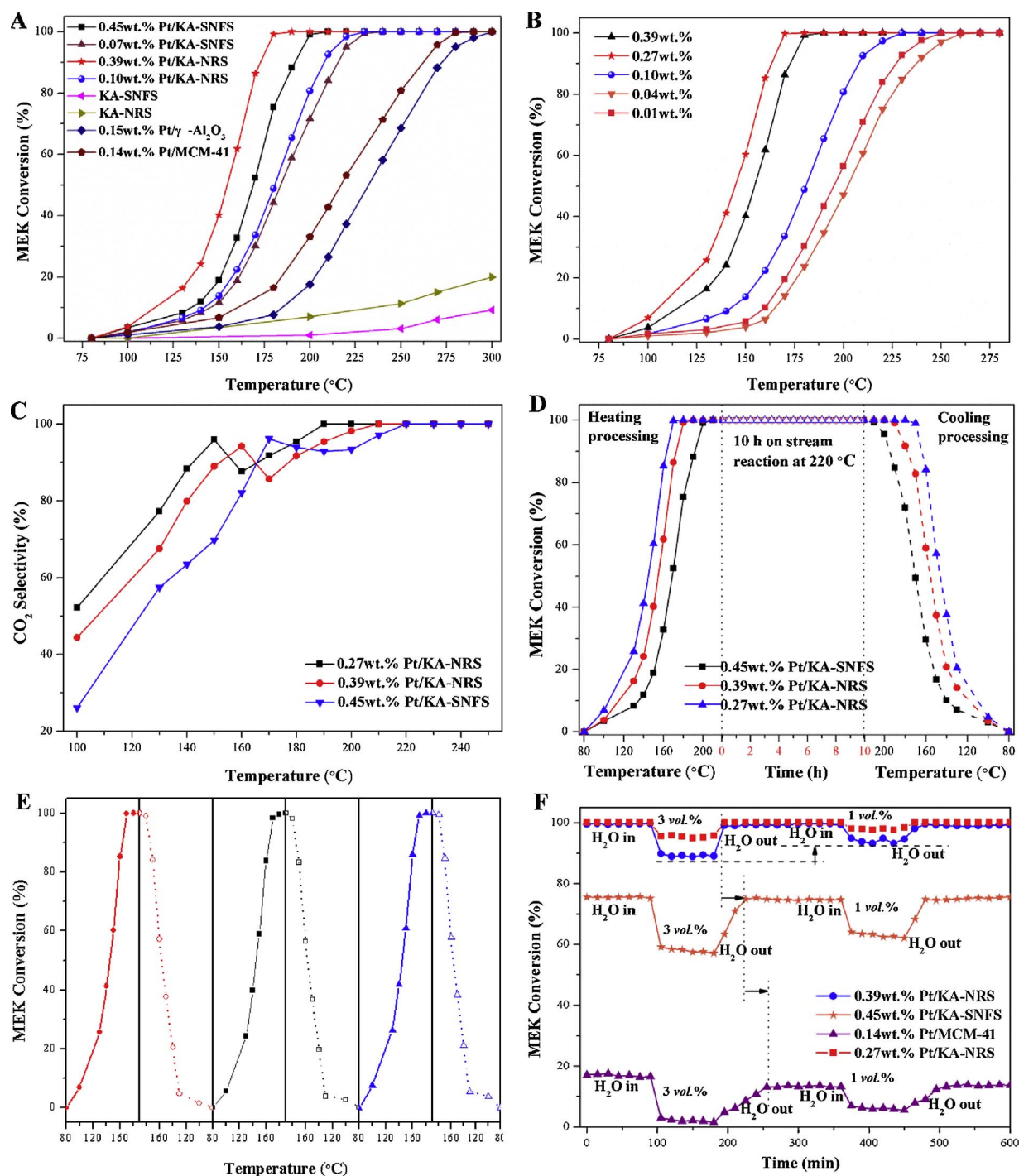


**Fig. 6.** (A) Catalytic activities for MEK combustion over different catalysts; (B) Catalytic activities for MEK combustion over KA-NRS with different Pt content; (C)  $\text{CO}_2$  selectivity of samples for MEK catalytic oxidation; (D) Stability test of active samples for MEK catalytic oxidation; (E) Circulation of heating and cooling process for MEK combustion; (F) Effect of 3 vol.% and 1 vol.% water vapor on MEK combustion at 180 °C.

values were ca. 16.2% and 14.5% for the 0.45 wt.% Pt/KA-SNFS and 0.14 wt.% Pt/MCM-41 sample, respectively. The temporary lose of activity indicates that the effect of water vapor in this reaction system is negative which may be due to the competitive adsorption of  $\text{H}_2\text{O}$ , MEK and  $\text{O}_2$  on the catalyst. The less reduce of MEK conversion demonstrates that 0.27 wt.% Pt/KA-NRS and 0.39 wt.% Pt/KA-NRS catalysts has better ability to resist the effect of water vapor than 0.14 wt.% Pt/MCM-41 and 0.45 wt.% Pt/KA-SNFS. When water vapor was cut off, the conversion of MEK restored to the original values for 0.27 wt.% Pt/KA-NRS, 0.39 wt.% Pt/KA-NRS, 0.45 wt.% Pt/KA-SNFS and 0.14 wt.% Pt/MCM-41 catalysts within 15, 30, 60 and 75 min, respectively, and kept

at 180 °C in the next 90 min. The recovery time for 0.14 wt.% Pt/MCM-41 is longest among all three samples, which are 45 min and 15 min longer than 0.39 wt.% Pt/KA-NRS and 0.45 wt.% Pt/KA-SNFS. Besides, it is difficult to maintain a stable level and the activity declines gradually after cutting off the water vapor. It verifies that the 3 vol.% water vapor has a significant negative effect on the traditional 0.14 wt.% Pt/MCM-41 catalyst. Subsequently, 1 vol.% water vapor was introduced into reaction, and the lose in activity decreases to 2.1%, 5.6%, 10.6% and 6.8% for the 0.27 wt.% Pt/KA-NRS, 0.39 wt.% Pt/KA-NRS, 0.45 wt.% Pt/KA-SNFS, and 0.14 wt.% Pt/MCM-41 catalysts, respectively, which can be respectively recovered in 15, 30, 30, and 45 min when the

**Table 2**  
Catalytic activities of all catalysts.

Sample	$T_5^a$ (°C)	$T_{50}^a$ (°C)	$T_{90}^a$ (°C)	$r_v^b$ (mmol·g <sub>Pt</sub> <sup>-1</sup> ·s <sup>-1</sup> )	TOF <sub>Pt</sub> <sup>c</sup> × 10 <sup>2</sup> (s <sup>-1</sup> )	$E_a^d$ (kJ·mol <sup>-1</sup> )
0.39 wt.% Pt/KA-NRS	104	154	172	5.22	2.39	48.41
0.27 wt.% Pt/KA-NRS	95	144	163	11.56	3.34	37.22
0.1 wt.% Pt/KA-NRS	123	181	208	8.14	2.29	39.67
0.04 wt.% Pt/KA-NRS	155	203	238	8.97	2.70	40.85
0.01 wt.% Pt/KA-NRS	146	195	227	5.72	14.93	47.63
0.45 wt.% Pt/KA-SNFS	111	168	192	4.41	9.97	53.41
0.07 wt.% Pt/KA-SNFS	128	184	216	10.63	10.19	41.96
0.14 wt.% Pt/MCM-41	140	218	263	2.71	1.81	55.92
0.15 wt.% Pt/γ-Al <sub>2</sub> O <sub>3</sub>	163	232	276	2.14	1.46	56.83

<sup>a</sup> Temperatures at which 5%, 50% and 90% conversion of MEK.

<sup>b</sup> Reaction rate of MEK molecules transformed per surface area per unit time of various catalysts at 110 °C.

<sup>c</sup> Turnover frequency based on the dispersion of Pt obtained at 110 °C.

<sup>d</sup> Apparent activation energy obtained from Arrhenius plot.

water vapor is removed.

The impact of MEK combustion decreases when reducing water vapor concentration. There are three main reasons for the superior stability of Pt/KA-NRS and Pt/KA-SNFS catalysts than traditional Pt/MCM-41. Firstly, the addition of K not only balances the negative charge of support, but also enhances the interaction between active sites and support; Secondly, the particle size of Pt nanoparticles over Pt/KA-NRS and Pt/KA-SNFS are small (2.6 nm of Pt/KA-NRS and 4.3 nm of Pt/KA-SNFS) and well-dispersed (keeping long distance between two active sites), which effectively prevented the aggregation of Pt nanoparticles during thermal treatment. Finally, Al atoms were incorporated into the silica framework by coordinating with silanol groups, resulting in fewer silanol groups and, therefore, were more resistant to hydrolysis under steaming conditions [13]. The superior stability of Pt/KA-NRS also confirmed by XPS spectra (Pt 4f + Al 2p) and XRD pattern of the fresh and used 0.27 wt.% Pt/KA-NRS (Fig. S5).

### 3.4.3. Reaction rate, turnover frequency and apparent activation energy

It is insufficient to judge the catalytic activity of different catalysts just by comparing the light-off curve and CO<sub>2</sub> selectivity although these parameters are very important for catalyst evaluation and selection. Comparatively, the turnover frequency (Fig. S6), reaction rate and apparent activation energy (Fig. 7) are much more persuasive to clarify the intrinsic activity of a catalyst. We compared the performance of supported noble metal catalysts using the MEK consumption rate per gram of catalyst (based on Pt). As shown in Fig. 7A, 0.27 wt.% Pt/KA-NRS shows the highest reaction rate (11.56 mmol·g<sub>Pt</sub><sup>-1</sup>·s<sup>-1</sup> at 110 °C) for MEK oxidation, two times higher than over 0.39 wt.% Pt/KA-NRS (5.22 mmol·g<sub>Pt</sub><sup>-1</sup>·s<sup>-1</sup> at 110 °C). The reaction rate of the active catalysts for catalyzing of MEK are ranked as: 0.27 wt.% Pt/KA-NRS > 0.39 wt.% Pt/KA-NRS > 0.45 wt.% Pt/KA-SNFS > 0.14 wt.% Pt/MCM-41 > 0.15 wt.% Pt/γ-Al<sub>2</sub>O<sub>3</sub>, in consistent with that of the catalytic activity.

The apparent activation energy ( $E_a$ ) was introduced to compare the low-temperature activity of our samples, as the catalyst with the lower  $E_a$  value would facilitate MEK oxidation more readily. Notably, the apparent activation energy is usually determined at a conversion of 5–10%. Since a low concentration (800 ppm) of MEK was adopted in the present study, the heat generated due to the combustion of MEK at a conversion of 15% would be small and insignificant temperature gradients would exist in the catalyst bed, although MEK oxidation is highly exothermic. That is to say, the thermal effect is insignificant in the present study. By proper treating the data in Fig. 6A and B, the Arrhenius plots could be drawn and  $E_a$  values could be evaluated for each sample, as presented in Fig. 7B and Table 2. 0.27 wt.% Pt/KA-NRS (37.2 kJ·mol<sup>-1</sup>) < 0.39 wt.% Pt/KA-NRS (48.4 kJ·mol<sup>-1</sup>) < 0.45 wt.% Pt/KA-SNFS (53.4 kJ·mol<sup>-1</sup>) < 0.14 wt.% Pt/MCM-41 (55.9 kJ·mol<sup>-1</sup>) < 0.15 wt.% Pt/γ-Al<sub>2</sub>O<sub>3</sub> (56.8 kJ·mol<sup>-1</sup>). The 0.27 wt.% Pt/KA-NRS samples showed lowest  $E_a$  (37.2 kJ·mol<sup>-1</sup>),

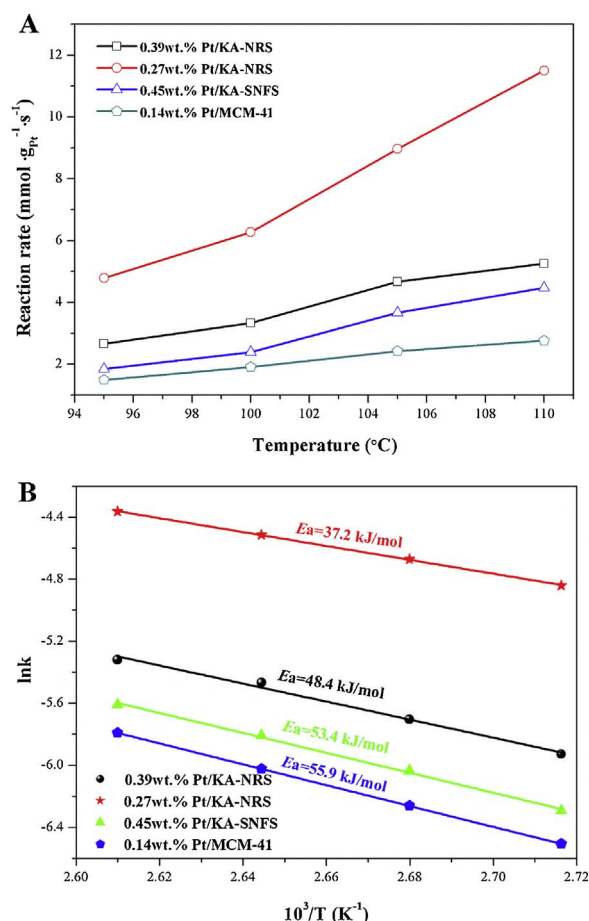
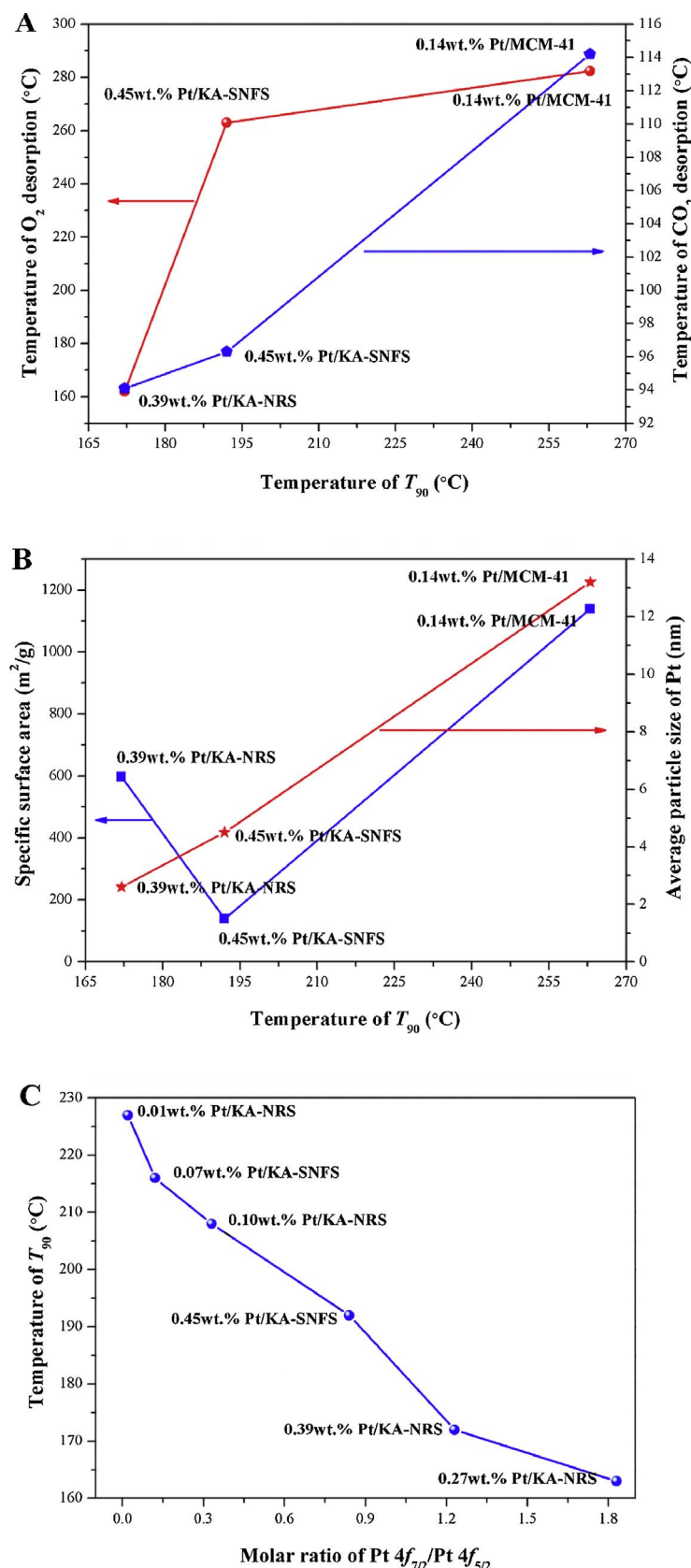


Fig. 7. (A) Reaction rates of some active samples; (B) Arrhenius plots of some active samples for MEK catalytic oxidation.

implying that MEK oxidation could proceed more readily.

## 4. Discussion

Nanorod silica (NRS) with high specific area and large pore volume was fabricated as a potential support. Pure silicate materials have an electrically neutral framework and consequently no Brønsted acid sites. When aluminum is incorporated into silicate framework, it is expected that the aluminum adopts tetrahedral coordination to four silicon atoms via oxygen bridges and yields so-called structural hydroxyls which serve as the Brønsted acid sites. The Brønsted acid sites can significantly promote Pt particle dispersion due to their electrophilic character [55],



**Fig. 8.** (A) The relation between catalytic activity and  $O_2$ -TPD/ $CO_2$ -TPD; (B) The relation between catalytic activity and specific surface area/particle size of Pt; (C) The relation between catalytic activity and molar ratio of Pt  $4f_{7/2}/Pt\ 4f_{5/2}$ .

and play an important role during MEK combustion. It promotes the adsorption of MEK over catalysts (Fig. S7 and Fig. S8) and provide proton for producing intermediate products.

For MEK oxidation on supported Pt catalysts, a number of

parameters, such as the particle size of active sites, specific surface area, adsorption capacity of  $O_2$  and  $CO_2$ , are thought to affect the catalytic performance. As shown in Fig. 8A, the  $O_2$  and  $CO_2$  desorption capabilities (Fig. S4B and Fig. S9) correlate positively to the MEK



combustion activity for 0.39 wt.% Pt/KA-NRS, 0.45 wt.% Pt/KA-SNFS and 0.14 wt.% Pt/MCM-41 samples. The  $T_{90}$  of these samples for MEK combustion increase with the decreasing of  $O_2$  and  $CO_2$  desorption temperatures. The addition of K promotes surface oxygen mobility, which desorbs and provides enough oxygen for catalytic oxidation. The desorption of  $CO_2$  which is the main product of the reaction and is directly promoted, releasing catalytic centers and the efficiency of MEK adsorption is improved, accelerating the catalytic reaction. From Fig. 8B, the specific surface areas do not correlate to the performance of MEK combustion. For instance, the 0.14 wt.% Pt/MCM-41 sample possesses a higher surface area than 0.39 wt.% Pt/KA-NRS and 0.45 wt.% Pt/KA-SNFS, but has the lowest activity. Nevertheless, the positive relationship between the average particle size of Pt nanoparticles and  $T_{90}$  can be observed (Fig. 8B). In this work, monodispersed Pt nanoparticles with small particle sizes is preferred, for example, the 0.39 wt.% Pt/KA-NRS catalyst with an average 2.6 nm Pt nanoparticles is more active than 0.45 wt.% Pt/KA-SNFS with 4.5 nm Pt nanoparticles. Furthermore, Fig. 8C illustrates the relationship between catalytic activity and molar ratio of Pt  $4f_{7/2}$ /Pt  $4f_{5/2}$  (Table S2). In this work, the peak component with binding energy around 71.2–71.5 eV of Pt  $4f_{7/2}$  and around 74.4–74.8 eV of Pt  $4f_{5/2}$  were divided in XPS Pt 4f spectra, all of them is the characteristic peak of metallic Pt<sup>0</sup>. However, the formation state of Pt nanoparticles in these two peaks is different. The first state is that Pt<sup>0</sup> is coordinated with K atoms, attributing to the peak position of Pt  $4f_{7/2}$ . Another state is that Pt<sup>0</sup> attached on the surface of support alone, which is ascribed to the peak position of Pt  $4f_{5/2}$ . A higher ratio of Pt  $4f_{7/2}$ /Pt  $4f_{5/2}$  represents a greater density of metallic Pt nanoparticles connecting with K atoms. Metallic Pt<sup>0</sup> nanoparticles that coordinate to K atoms are considered to be the preferred active sites rather than those on the surface of the support. K atoms in catalysts can balance the negative charge of the support and anchor Pt nanoparticles, which improves the interface between active sites and support. It indicates that the large proportion of metallic Pt<sup>0</sup> is in favor of MEK oxidation at lower temperatures, which is in line with the previous report [13].

The mechanism and reaction routes in MEK catalytic oxidation were explored with *in situ* DRIFTS experiment and DFT studies (Fig. S10), whereby, relative concentrations of MEK and products were detected by on-line MS (Fig. S11) and TPSR (Fig. S12). From Fig. 6C, the decrease in MEK concentration and increase in  $CO_2$  concentration, as well as no CO formation (not shown), are seen as a function of reaction temperature for all the catalysts. The implication is that  $CO_2$  is the main product of MEK catalytic oxidation in our work.

From Fig. 9A, the negative peak at  $3755\text{ cm}^{-1}$  and the positive peak at  $3734\text{ cm}^{-1}$  observed at wavelengths between 3500 and  $4000\text{ cm}^{-1}$  are ascribed to acid sites on catalyst and surface hydroxyl groups, respectively [56]. The surface hydroxyl groups can be assigned to 2-butanol and 2,3-butandiol. MEK molecules are absorbed on the acid sites of catalysts at the beginning of the reaction and consequently oxidized by Pt<sup>0</sup> upon increasing temperatures. Therefore, we consider the vibration of greater exposed acid sites to be strengthened. Additionally, a broad and strong peak at  $3262\text{ cm}^{-1}$  is attributed to the stretching vibration of adsorbed water, which is mainly due to the combustion of MEK [56]. The peaks at  $2372\text{ cm}^{-1}$  and  $2310\text{ cm}^{-1}$  are assigned to the stretching vibration of  $CO_2$ , which is the main product of during MEK catalytic oxidation [57]. These peaks show a tendency to gradually increase as the reaction temperature approaches  $200^\circ\text{C}$ , which coincides with the  $CO_2$  selectivity (Fig. 6C). Three peaks at  $2991\text{ cm}^{-1}$ ,  $2949\text{ cm}^{-1}$  and  $2888\text{ cm}^{-1}$  are detected and ascribed to the bending vibration and stretching vibration of C–H [58]. Two peaks at  $1588\text{ cm}^{-1}$  and  $1435\text{ cm}^{-1}$  are detected and attributed to the stretching vibration of C–C [59]. The presence of  $\nu(C-H)$  and  $\nu(C-C)$  bands may be ascribed to the adsorbed residual hydrocarbon fragments, derived from MEK decomposition. The peak detected at  $1716\text{ cm}^{-1}$  corresponds to diacetyl which is assigned to C=O normally [60]. The peak at  $1352\text{ cm}^{-1}$  is assigned to the vibration of  $-CH_3$  of acetaldehyde and

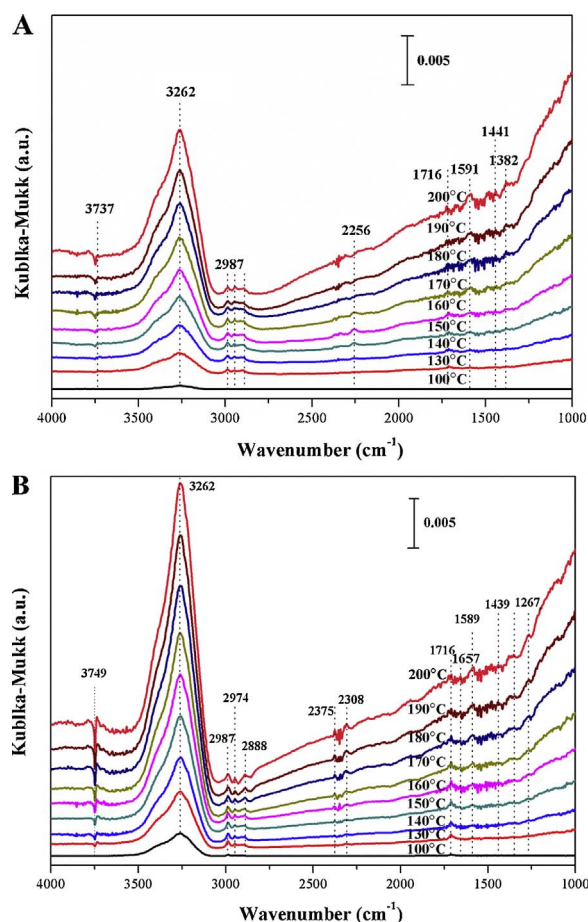


Fig. 9. *In situ* DRIFTS spectra of (A) 0.39 wt.% Pt/KA-NRS and (B) 0.45 wt.% Pt/KA-SNFS catalysts for MEK catalytic oxidation as a function of temperature in flowing MEK +  $N_2$  +  $O_2$  from 100 to  $200^\circ\text{C}$ .

acetic acid [59]. Moreover, the peaks at  $1477\text{ cm}^{-1}$  and  $1267\text{ cm}^{-1}$  are clearly observed at high temperature, which corresponds to formic acid and formaldehyde [22].

According to Fig. 9B, similarly for the 0.45 wt.% Pt/KA-SNFS sample, the negative peak at  $3750\text{ cm}^{-1}$  and the positive peak at  $3262\text{ cm}^{-1}$  observed at wavelengths between 3000 and  $4000\text{ cm}^{-1}$  are ascribed to acid sites of catalyst and surface adsorbed water, respectively. The peaks at  $2995\text{ cm}^{-1}$ ,  $2951\text{ cm}^{-1}$  and  $2889\text{ cm}^{-1}$  are ascribed to  $\nu(C-H)$ , and the peaks at  $1591\text{ cm}^{-1}$  and  $1444\text{ cm}^{-1}$  are attributed to  $\nu(C-C)$ . The peak of C=O vibration from diacetyl is detected at  $1716\text{ cm}^{-1}$ . However, the peak detected at  $2256\text{ cm}^{-1}$  can be assigned to the vibration of CO [24]. The intensity of this vibration gradually increases at low temperature and disappears when the temperature above  $160^\circ\text{C}$ . It can be concluded that CO is formed at low temperature, which leads to a lower  $CO_2$  selectivity on 0.45 wt.% Pt/KA-SNFS.

Based on the above structural and composition analyses of the obtained Pt/KA-NRS catalyst as well as the observed catalysis in MEK oxidation, the potential mechanism for MEK combustion over 0.27 wt.% Pt/KA-NRS are proposed in Fig. 10. The MEK molecules are firstly adsorbed on the Brønsted acidic sites of the catalyst surface. The monodispersed metallic Pt nanoparticles connected with K are active sites for MEK combustion. Accordingly, two reaction routes are proposed, which are slight different from the previous report. Along with the participation of surface adsorbed oxygen and the Brønsted acidic sites, MEK transforms into 2,3-butandiol and diacetyl through 2-butanol and acetoin as intermediate products. The 2,3-butandiol as an intermediate is oxidatively cleaved to form acetaldehyde and diacetyl cleaved to form acetaldehyde and acetic acid. Acetaldehyde and acetic

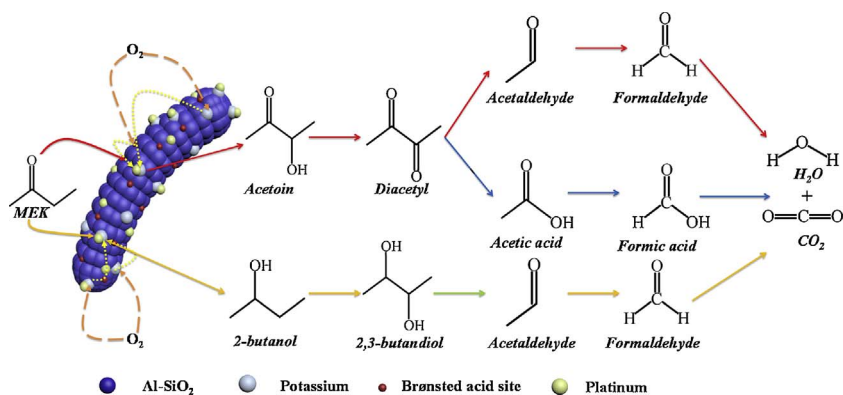


Fig. 10. Schematic of reaction mechanism for MEK catalytic oxidation over 0.27 wt.% Pt/KA-NRS.

acid are considered the primary C<sub>2</sub> scission product of MEK, which further convert into formaldehyde and formic acid with the help of the Brønsted acid sites before completely oxidized to CO<sub>2</sub> and H<sub>2</sub>O.

## 5. Conclusions

In this work, hierarchically micro-mesostructured K-Al-SiO<sub>2</sub> supports with regular nanorod (KA-NRS) and spherical nanoflower-like (KA-SNFS) morphologies were prepared. Monodispersed Pt nanoparticles were supported on KA-NRS and KA-SNFS through the ethylene glycol reduction and colloid impregnation methods. The addition of Al atoms produces Brønsted acid sites and reduces silanol groups over supports, promoting the dispersion of Pt nanoparticles and the stability of the catalysts. The Pt/KA-NRS catalysts exhibit unexceptionable low temperature activity, CO<sub>2</sub> selectivity and stability for MEK oxidation. The excellent catalytic activity of Pt/KA-NRS for MEK oxidation can be ascribed to the regular morphology of the support and high dispersion of Pt nanoparticles. Furthermore, the average particle size of Pt nanoparticles, O<sub>2</sub> and CO<sub>2</sub> desorption temperatures have positive correlation to the activity for MEK combustion. *In situ* DRIFTS and DFT results reveal that diacetyl and 2,3-butandiol are the main intermediates during MEK activation, which convert into H<sub>2</sub>O and CO<sub>2</sub> through aldehydes and acids. It can be reasonably anticipated that the Pt/KA-NRS catalyst system should be a promising candidate for low-temperature catalytic oxidation of VOCs.

## Acknowledgements

This work was financially supported by the National Natural Science Foundation of China (21477095, 21677114, 21337003), the National Key Research and Development Program (2016YFC0204201), the Natural Science Basic Research Plan in Shaanxi Province of China (2014JQ2-2009), and the Fundamental Research Funds for the Central Universities (xjj2017170). The authors also appreciate the editor and reviewers for their professional work and valuable comments.

## Appendix A. Supplementary data

Supplementary data associated with this article can be found, in the online version, at <https://doi.org/10.1016/j.apcatb.2017.12.007>.

## References

- M.Y. Mao, Y.Z. Li, J.T. Hou, M. Zeng, X.J. Zhao, *Appl. Catal. B: Environ.* 174–175 (2017) 496–503.
- P. Lakshmanan, L. Delannoy, V. Richard, C. Méthivier, C. Potvin, C. Louis, *Appl. Catal. B: Environ.* 96 (2010) 117–125.
- C.H. Zhang, C. Wang, S. Gil, A. Boreave, L. Retaillieu, Y.L. Guo, J.L. Valverde, A. Giroir-Fendle, *Appl. Catal. B: Environ.* 201 (2017) 552–560.
- S. Scire, L.F. Liotta, *Appl. Catal. B: Environ.* 125 (2012) 222–246.
- J.J. Zhu, T. Wang, X.L. Xu, P. Xiao, J.L. Li, *Appl. Catal. B: Environ.* 130–131 (2013) 197–217.
- L.H. Nie, J.G. Yu, M. Jaroniec, F.F. Tao, *Catal. Sci. Technol.* 6 (2016) 3649–3669.
- W.F. Tu, Y.H. Chin, *Angew. Chem. Int. Ed.* 53 (2014) 12148–12152.
- S. Royer, D. Duprez, F. Can, X. Courtois, C. Batiot-Dupeyrat, S. Laassiri, H. Alamdari, *Chem. Rev.* 114 (2014) 10292–10368.
- L.F. Liotta, *Appl. Catal. B: Environ.* 100 (2010) 403–412.
- J.J. Zhu, T. Wang, X.L. Xu, P. Xiao, J.L. Li, *Appl. Catal. B: Environ.* 130–131 (2013) 197–217.
- Z. Vít, D. Gulková, L. Kaluža, M. Boaro, *Appl. Catal. B: Environ.* 146 (2014) 213–220.
- B. Darif, S. Ojala, L. Pirault-Roy, M. Bensitel, R. Brahmi, R.L. Keiski, *Appl. Catal. B: Environ.* 181 (2016) 24–33.
- C.Y. Chen, Q.M. Wu, F. Chen, L. Zhang, S.X. Pan, C.Q. Bian, X.M. Zheng, X.J. Meng, F.-S. Xiao, *J. Mater. Chem. A* 3 (2015) 5556–5562.
- H. Huang, Q.G. Dai, X.Y. Wang, *Appl. Catal. B: Environ.* 158–159 (2014) 96–105.
- Y.B. Li, C.B. Zhang, H. He, J.H. Zhang, M. Chen, *Catal. Sci. Technol.* 6 (2016) 2289–2295.
- C. Zhang, F. Liu, Y. Zhai, H. Ariga, N. Yi, Y. Liu, K. Asakura, M. Flytzani-Stephanopoulos, H. He, *Angew. Chem. Int. Ed.* 51 (2012) 9628–9632.
- G. Arzamendi, V.A. Peña O'Shea, M.C. Álvarez-Galván, J.L.G. Fierro, P.L. Arias, L.M. Gandía, *J. Catal.* 261 (2009) 50–59.
- A. Gil, M.A. Vicente, J.-F. Lamnert, L.M. Gandía, *Catal. Today* 68 (2001) 41–51.
- M. Guilemot, J. Mijoin, S. Mignard, P. Magnoux, *Appl. Catal. B: Environ.* 75 (2007) 249–255.
- L. Yue, C. He, X. Zhang, P. Li, Z. Wang, H. Wang, Z.P. Hao, *J. Hazard. Mater.* 244–245 (2013) 613–620.
- H. Pan, Y.F. Jian, C.W. Chen, C. He, Z.P. Hao, H.X. Liu, Z.X. Shen, *Environ. Sci. Technol.* 51 (2017) 6288–6297.
- Y.T. Lai, T.C. Chen, Y.K. Lan, B.S. Chen, J.H. You, C.M. Yang, N.C. Lai, J.H. Wu, C.S. Chen, *ACS Catal.* 4 (2014) 3824–3836.
- J.T. Tompkins, R. Mokaya, *ACS Appl. Mater. Interfaces* 6 (2014) 1902–1908.
- B. Çelik, E. Erken, S. Eriş, Y. Yıldız, B. Şahin, H. Pamuk, F. Sen, *Catal. Sci. Technol.* 6 (2016) 1685–1692.
- R.D. Zhang, N.L. Shi, B.H. Chen, *Appl. Catal. B: Environ.* 146 (2014) 79–93.
- Y.D. Wang, Z.C. Tao, B.S. Wu, J. Xu, C.F. Huo, K. Li, H.M. Chen, Y. Yang, Y.M. Li, *J. Catal.* 322 (2015) 1–13.
- Z.H. Xu, J.G. Yu, M. Jaroniec, *Appl. Catal. B: Environ.* 163 (2015) 306–312.
- X. Huang, Y. Men, J. Wang, W. An, Y. Wang, *Catal. Sci. Technol.* 7 (2017) 168–180.
- P. Claus, S. Schimpf, R. Schödel, P. Kraak, W. Mörke, D. Hönicke, *Appl. Catal. A: Gen.* 165 (1997) 429–441.
- T. Ishiyama, T. Fukuda, Y. Yamashita, Y. Kamiura, *Physica B* 376–377 (2006) 89–92.
- J. Michalik, D. Brown, J.-S. Yu, M. Danilczuk, J.Y. Kim, L. Kevan, *Phys. Chem. Chem. Phys.* 3 (2001) 1705–1708.
- K.C. Petalidou, A.M. Efstathiou, *Appl. Catal. B: Environ.* 140–141 (2013) 333–347.
- S. Gomez, L. Lerici, C. Saux, A.L. Perez, C.D. Brondino, L. Pierella, L. Pizzio, *Appl. Catal. B: Environ.* 202 (2017) 580–586.
- J. Wisniewska, M. Ziolk, *RSC Adv.* 7 (2017) 9534–9544.
- S. Zuo, X. Wang, P. Yang, C. Qi, *Catal. Commun.* 94 (2017) 52–55.
- J.A.C. Ruiz, E.C. Oliveira, M.A. Fraga, H.O. Pastore, *Catal. Commun.* 25 (2012) 1–6.
- J. Czaplinska, P. Decyk, M. Ziolk, *Appl. Catal. A: Gen.* 504 (2015) 361–372.
- F. Morfin, T.-S. Nguyen, J.-L. Rousset, L. Piccolo, *Appl. Catal. B: Environ.* 197 (2016) 2–13.
- K.A. Almeida, R. Landers, D. Cardoso, *J. Catal.* 294 (2012) 151–157.
- J. Dou, B.W. Zhang, H. Liu, J.D. Hong, S.M. Yin, Y.Z. Huang, R. Xu, *Appl. Catal. B: Environ.* 180 (2016) 78–85.
- I.S. Chae, M. Kim, Y.S. Kang, S.W. Kang, *J. Membrane Sci.* 466 (2014) 357–360.
- A.M. Hibberd, S.L. Bergman, Y.L. Zhong, S.L. Bernasek, *J. Chem. Phys.* 137 (2012) 1–8.
- A.K. Medina-Mendoza, M.A. Cortés-Jácome, J.A. oledo-Antonio, C. Angeles-Chávez, E. López-Salinas, I. Cuauhtémoc-López, M.C. Barrera, J. Escobar, J. Navarrete, I. Hernández, *Appl. Catal. B: Environ.* 106 (2011) 14–25.
- J. Scott, W. Irawaty, G. Low, R. Amal, *Appl. Catal. B: Environ.* 164 (2015) 10–17.
- H.Y. Zhao, D.W. Wang, C.B. Gao, H.Y. Liu, L. Han, Y.D. Yin, *J. Mater. Chem. A* 4 (2016) 1366–1372.
- Q.D. Zhang, Y.S. Tan, G.B. Liu, J.F. Zhang, Y.Z. Han, *Green Chem.* 16 (2014)

- 4708–4715.
- [47] J.N. Kim, W.D. Kim, Y.B. Seo, J.C. Kim, R. Ryoo, *J. Catal.* 310 (2013) 187–197.
- [48] H.-C. Wu, T.-C. Chen, N.-C. Lai, C.-M. Yang, J.-H. Wu, Y.-C. Chen, J.-F. Lee, C.-S. Chen, *Nanoscale* 7 (2015) 16848–16859.
- [49] S. Shen, X.L. Wang, Q. Ding, S.Q. Jin, Z.C. Feng, C. Li, *Chin. J. Catal.* 35 (2014) 1900–1906.
- [50] J. Wan, R. Ran, M. Lin, X.D. Wu, D. Weng, *J. Mol. Catal. A: Chem.* 383–384 (2014) 194–202.
- [51] M.J.S. Farias, C. Busó-Rogero, R. Gisbert, E. Herrero, J.M. Feliu, *J. Phys. Chem. C* 118 (2014) 1925–1934.
- [52] J. Winsniewska, M. Ziolek, N. Artioli, M. Daturi, *J. Catal.* 336 (2016) 58–74.
- [53] M.J. Kale, P. Christopher, *ACS Catal.* 6 (2016) 5599–5609.
- [54] X.L. Zou, Z.B. Rui, S.Q. Song, H.B. Ji, *J. Catal.* 338 (2016) 192–201.
- [55] A.X.Y. She, J.H. Kwak, J.M. Sun, J.Z. Hu, M.Y. Hu, C.M. Wang, C.H.F. Peden, Y. Wang, *ACS Catal.* 2 (2012) 1020–1026.
- [56] D.W. Kwon, P.W. Seo, G.J. Kim, S.C. Hong, *Appl. Catal. B: Environ.* 163 (2015) 436–443.
- [57] C.Y. Ma, G.L. Pang, G.Z. He, Y. Li, C. He, Z.P. Hao, *J. Environ. Sci.* 39 (2016) 77–85.
- [58] X.L. Zou, Z.B. Rui, S.Q. Song, H.B. Ji, *J. Catal.* 338 (2016) 192–201.
- [59] C. He, Y.K. Yu, J.W. Shi, Q. Shen, J.S. Chen, H.X. Liu, *Mater. Chem. Phys.* 157 (2015) 87–100.
- [60] Z.H. Xu, J.G. Yu, M. Jaroniec, *Appl. Catal. B: Environ.* 163 (2015) 306–312.